

INORGANIC CHEMISTRY

FRONTIERS

RESEARCH ARTICLE

View Article Online

View Journal | View Issue



Cite this: *Inorg. Chem. Front.*, 2016, **3**, 1501

Two-dimensional nanostructures of non-layered ternary thiospinels and their bifunctional electrocatalytic properties for oxygen reduction and evolution: the case of CuCo_2S_4 nanosheets†

Shulin Zhao,^{‡a} Yu Wang,^{‡a} Qinghua Zhang,^{b,c} Yafei Li,^a Lin Gu,^b Zhihui Dai,^a Suli Liu,^a Ya-Qian Lan,^a Min Han^{*a} and Jianchun Bao^{*a}

Two-dimensional (2D) transition metal chalcogenide nanostructures exhibit unique electronic, opto-electronic and mechanical properties, showing great potential for innovation of future electronics, renewable energy, sensing, and catalysis fields. Despite achieving great progress, fabricating 2D nanostructures of non-layered ternary thiospinels remains a great challenge, and their bifunctional electrocatalytic properties toward both oxygen reduction and evolution reactions (ORR and OER) have not been explored. In this paper, 2D nanostructures of an earth-abundant non-layered ternary thiospinel compound – CuCo_2S_4 nanosheets (NSs) – with their (111), (022) and (004) planes mainly exposed, are synthesized via a “leveling metal activity and structure-directed one-pot sulfurization” strategy. The electrocatalytic tests in alkaline solution show that such CuCo_2S_4 NSs can efficiently catalyze both the ORR and OER, whose bifunctional catalytic properties are superior to binary metal sulfide nanostructures, Pt/C, CuCo_2S_4 nanoparticles, and recently reported some bifunctional oxygen-electrode catalysts (e.g. $\text{Co}_x\text{S}_y\text{@C-1000}$, N-doped G/CNTs, $\text{Co}_3\text{O}_4/\text{NBGHSS}$, CoFe_2O_4 , $\text{Co}_x\text{Mn}_{3-x}\text{O}_4$, MnO_x , NiCo_2S_4 hollow spheres, $\text{NiCo}_2\text{S}_4\text{@N/S-rGO}$, etc.). Combined with spin-polarized density functional theory computations based on a computational hydrogen electrode model, their excellent bifunctional catalytic properties originate from the presence of the two special facets, (022) and (004), which have different preferences in terms of the ORR/OER. This work not only enriches the current 2D material family but also paves the way for rational design of advanced multifunctional 2D electrocatalysts for use in renewable energy fields.

Received 3rd September 2016,
Accepted 30th September 2016

DOI: 10.1039/c6qi00355a

rsc.li/frontiers-inorganic

Introduction

Two-dimensional (2D) transition metal chalcogenide (TMC) nanostructures have been attracting considerable attention^{1,2} owing to their promising applications in opto-electronics,³ energy storage,⁴ sensing,⁵ and catalysis.^{6,7} For catalytic application, their performances can be modulated through engineering surface defects, strains, thickness, phase structures and

components,^{8–11} elemental doping,^{12,13} surface modification,¹⁴ enhancing electric conductivity,^{15–17} forming hybrid materials¹⁸ and morphology control.^{19–21} For instance, by tuning the components, the ternary TMC nanosheets (NSs), e.g., $\text{MoS}_{2(1-x)}\text{Se}_{2x}$ and $\text{WS}_{2(1-x)}\text{Se}_{2x}$, show greatly enhanced electrocatalytic performance in contrast to their binary counterparts.^{22,23} Among numerous ternary TMCs, thiospinels with two kinds of metal cations occupy the tetrahedral and octahedral vacancies of a closely-packed S anionic lattice, retain a large ionic character and show good metallic conductivity,²⁴ offering a robust library to screen high-performance electrocatalytic materials. It is reported that ultrathin NS structures can increase the available active sites and improve the electronic conductivity of a desired catalyst,^{25,26} which inspires us to fabricate ultrathin ternary thiospinel NSs with the dream to find advanced electrocatalysts for use in renewable energy fields. Nonetheless, due to their non-layered crystalline structure or strong chemical bonding in three dimensions, it is difficult to obtain ultrathin ternary thiospinel NSs *via* conventional exfoliation or intercalation strategies. Though some wet-

^aJiangsu Key Laboratory of Biofunctional Materials, School of Chemistry and Materials Science, Nanjing Normal University, Nanjing 210023, P. R. China.
E-mail: 07203@njnu.edu.cn, baojianchun@njnu.edu.cn; Fax: +86-25-85891051;
Tel: +86-25-85891051

^bBeijing National Laboratory for Condensed Matter Physics, Institute of Physics, Chinese Academy of Sciences, Beijing 100190, P. R. China

^cDepartment of Materials Science and Engineering, Tsinghua University, Beijing 100084, P. R. China

†Electronic supplementary information (ESI) available: EDS pattern and AFM image, characterization of control samples and catalysts, and additional electrochemical data. See DOI: 10.1039/c6qi00355a

‡These authors contributed equally.

chemical routes, such as solvothermal and soft colloidal template methods, have been used to prepare non-layered binary TMC NSs,²⁷ they are not successfully developed for ternary thiospinels. This could be due to the diverse reactivity of metal cations that induce “secondary” nucleation to form phase-separated products and affect the growth dynamic process. So, it is imperative but challenging to develop an efficient avenue for the fabrication of ultrathin ternary thiospinel NSs.

As a member of ternary thiospinels, CuCo_2S_4 naturally exists in carrollite and has unique oxidation states for Cu (+1) and Co (+2.4) ions,²⁸ unlike normal thiospinel compounds. Also, it possesses s-wave superconductivity at low temperature and exhibits a quite low resistivity ($10^{-4} \Omega$) under ambient conditions,²⁹ which has been used as the cathode material in Li-ion batteries.^{30,31} Very recently, some CuCo_2S_4 nanostructures, such as nanoparticles and hierarchical hollow nanoneedle arrays, have been synthesized and found to be excellent electroactive materials for supercapacitors^{32–34} or quantum-dot sensitized solar cells.³⁵ Additionally, the CuCo_2S_4 nanoparticles are yet to be identified as a good electrocatalyst for the oxygen evolution reaction (OER).³⁶ Unfortunately, by far, there is still no report on CuCo_2S_4 NSs and their electrocatalytic properties remain unknown. Considering that Cu- and Co-based nanocrystals are good electrocatalysts toward the oxygen reduction reaction (ORR)³⁷ and OER,^{38–40} respectively, and the 2D CuCo_2S_4 NSs may provide good opportunity for exposing two or more special facets with different active sites, they are expected to show newly or enhanced bifunctional catalytic activity for both the ORR and OER. Based on these considerations, synthesizing CuCo_2S_4 NSs and examining their electrocatalytic ORR and OER properties become an interesting topic, which is important for exploring advanced multifunctional electrocatalysts for use in many renewable energy options.^{41–45}

Here, we report the synthesis of CuCo_2S_4 NSs and their bifunctional electrocatalytic properties for both the ORR and OER. In view of its non-layered crystalline structure, the “bottom-up” route is the better choice for obtaining CuCo_2S_4 NSs, *i.e.*, the Cu and Co ions co-exist in the solution that is subjected to sulfurization. However, the sulfurization rates or reactivity of Cu and Co ions are quite different since they have distinct affinity for the S element. For obtaining phase-pure CuCo_2S_4 NSs, the reactivity of Cu and Co ions should be leveled. To this end, the ligands in Cu and Co precursors are vital. Usually, the stronger the ligands, the better they are for leveling metal ions’ reactivity and controlling the crystallographic growth direction.⁴⁶ By taking advantage of the strong acetylacetonate ligand to chelate Cu and Co ions and utilizing 1-dodecanethiol (DDT) as the sulfur source and structure-directing reagent, the reactivity of Cu and Co ions can be efficiently leveled, leading to form phase-pure CuCo_2S_4 NSs. Thus, we call our method as a “leveling metal reactivity and structure-directed one-pot sulfurization” strategy. The CuCo_2S_4 NSs thus obtained mainly expose the (111), (022) and (004) planes, whose average thickness is about 10–13 nm. Combined with spin-polarized density functional theory (DFT) compu-

tations based on the computational hydrogen electrode (CHE) model, the two exposed (022) and (004) planes have different preferences in terms of the ORR/OER. As a result, in alkaline solution, the CuCo_2S_4 NSs exhibit excellent bifunctional catalytic properties toward both the ORR and OER. For the ORR, the onset reduction potential and half-wave potential are 0.90 and 0.74 V (*vs.* RHE), respectively. And for the OER, the onset oxidation potential is 1.5 V (*vs.* RHE) and a very small overpotential (0.337 V) is observed at a current density of 10 mA cm^{-2} . Based on the potential drop between the OER current density at 10 mA cm^{-2} and the ORR half-wave potential, the bifunctional catalytic performances of such CuCo_2S_4 NSs are superior to binary metal sulfides, commercial Pt/C, CuCo_2S_4 nanoparticles and recently reported bifunctional oxygen electrocatalysts (*e.g.* $\text{Co}_x\text{S}_y\text{@C-1000}$, N-doped G/CNTs, $\text{Co}_3\text{O}_4/\text{NBGHSS}$, CoFe_2O_4 , $\text{Co}_x\text{Mn}_{3-x}\text{O}_4$, $\text{LaCoO}_{3-\delta}$, MnO_x , NiCo_2S_4 hollow spheres, $\text{NiCo}_2\text{S}_4\text{@N/S-rGO}$, $\text{Co}_3\text{O}_4/2.7\text{Co}_2\text{MnO}_4$, $\text{Ni}_{0.6}\text{Co}_{2.4}\text{O}_4$, $\text{MnCo}_2\text{O}_4/\text{C}$, LDO/CNTs , N-doped G mesh),^{43–45,47–58} and close to Co NP@NC/NG-700.⁵⁹ To the best of our knowledge, the CuCo_2S_4 NSs are the best one in the current spinel-structured bifunctional oxygen electrocatalysts family, showing great potential for use in regenerative $\text{H}_2\text{-O}_2$ fuel cells or metal-air batteries.

Experimental

Materials

Except for the special illustration, all chemical reagents were purchased from Aldrich without further purification. The commercial Pt/C (20%) catalyst was bought from Alfa Aesar.

Synthesis of CuCo_2S_4 NSs

In a typical synthesis, 0.081 g of copper acetylacetonate ($\text{Cu}(\text{acac})_2$) and 0.154 g of cobalt acetylacetonate ($\text{Co}(\text{acac})_2$) were dissolved in 10 mL of dodecylamine at 120 °C to form a homogeneous solution. Then, 1.2 mL of DDT was quickly injected into the above solution. Subsequently, the mixture was heated to 245 °C at a rate of 5 °C min^{-1} and maintained at 245 °C for 10 min. After being allowed to cool naturally to room temperature, the crude product was separated by centrifugation and washed with *n*-heptane and ethanol several times to remove the by-products. Finally, the CuCo_2S_4 NSs thus obtained were dried at 40 °C in a vacuum for 2 h.

Synthesis of CuCo_2S_4 nanoparticles

The synthetic process was similar to CuCo_2S_4 NSs. The only difference was that thioacetamide was used as the sulfur resource to replace DDT.

Synthesis of binary metal sulfide nanostructures

The synthesis of Cu_7S_4 nanodisks and Co_3S_4 nanocrystal control catalysts was similar to CuCo_2S_4 NSs. The difference was that only $\text{Cu}(\text{acac})_2$ or $\text{Co}(\text{acac})_2$ was used as the metal precursor.

Materials characterization

The X-ray diffraction patterns (XRD) were collected on a D/max 2500 VL/PC diffractometer equipped with graphite-monochromatized Cu K α radiation ($\lambda = 1.54060 \text{ \AA}$). The working voltage and current are 40 kV and 100 mA, respectively. The X-ray energy dispersive spectra (EDS) were recorded on a JSM-5610LV-Vantage type energy spectrometer. The samples were dispersed on clean Al sheets for the EDS test. The Raman spectra were recorded on a JY HR 800 (France) instrument with an optical multichannel spectrometer equipped with a microscope. An objective with $\times 100$ magnification was used both for focusing the excitation light (Ar⁺ laser, 488 nm) and for collecting the scattered light. The X-ray photoelectron spectra (XPS) were obtained on a scanning X-ray microprobe (PHI VersaProbe 5000, ULVAC-PHI, Inc.) using Al K α radiation. The binding energies for various elements were calibrated using the C 1s peak (BE = 284.6 eV) as a standard. The field-emission scanning electron microscopy (FE-SEM) images were obtained on a JSM-7600F apparatus at an accelerating voltage of 10 kV. The samples were dispersed on clean Al sheets (>99.99%) for FE-SEM analysis without sputtering Au. The charge-free mode was employed to collect the FE-SEM images. The atomic force microscopy (AFM) studies were performed by means of a Nanoscope IIIa Scanning Probe Microscope (Agilent, USA) using the tapping mode. And the transmission electron microscopy (TEM) imaging was carried out on a JEOL-2100F apparatus at an accelerating voltage of 200 kV, which is equipped with STEM and X-ray energy dispersive spectrum detectors. Finally, the high-resolution TEM (HRTEM) images were obtained using an ARM-200CF transmission electron microscope operated at 200 kV and equipped with double spherical aberration correctors.

Electrocatalytic measurements

The electrocatalytic tests were carried out on a Gamry's rotating disk electrode (RDE) with a glassy disk (5 mm in diameter) that was equipped with the CHI 700e electrochemical workstation. A standard three-electrode system was used for all the tests. The Ag/AgCl and Pt foil were used as reference and counter electrodes, respectively. The catalyst modified RDEs were used as the working electrodes. These were fabricated according to the following procedure: 2.5 mg of CuCo₂S₄ NSs or other related samples were dispersed in 1 mL of ethanol and water, and 40 μL of 5.0 wt% Nafion® solution to form a homogeneous catalyst ink. A total of 16 μL of this catalyst ink was coated on pre-treated RDEs using a microliter syringe. After drying, the catalyst modified RDEs were fabricated. In all the experiments, the total loading amount of various catalysts was fixed to be 40 μg . For the ORR tests, the polarization curves were recorded in the O₂-saturated 0.1 M KOH electrolyte from -0.8 to 0.1 V (vs. Ag/AgCl) at different rotation rates. And for the OER tests, the polarization curves were recorded at 0 to 1.0 V (vs. Ag/AgCl) with an electrode rotation rate of 1600 rpm. These polarization plots were corrected for solution resistance. The resistance of 0.1 M KOH is $\sim 42 \Omega$.

In this work, all potentials were converted to reversible hydrogen electrode (RHE) values. The formula: $E(\text{RHE}) = E(\text{Ag}/\text{AgCl}) + 0.973 \text{ V}$, was used for calibrating the work potential. The calibration was carried out according to a previous report.⁶⁰

Theoretical computations

The spin-polarized DFT computations were performed using the plane-wave technique implemented in the Vienna *ab initio* Simulation package (VASP),⁶¹ with exchange-correlation interactions modeled by the Perdew–Burke–Ernzerhof (PBE) generalized gradient approximation (GGA) function.⁶² The ion–electron interaction is modeled using the projector-augmented plane wave (PAW) approach.⁶³ A plane-wave cutoff energy of 360 eV was adopted in all computations. The Brillouin zone was sampled with $3 \times 4 \times 1$ for (022) planes and $4 \times 4 \times 1$ k -points for (004) as well as (111) planes. Besides, the electronic structure calculations were employed with a Fermi-level smearing of 0.1 and 0.01 eV for surfaces and gas-phase species calculations, respectively. The convergence threshold was conducted with 10^{-4} eV energy and 0.02 eV \AA^{-1} force, and a vacuum region of around 15 \AA was set along the Z-direction to avoid the interaction between periodic images. Other details for computations are given in the ESI.†

Results and discussion

Fig. 1A shows the powder XRD pattern of the as-synthesized CuCo₂S₄ NSs, from which seven distinct diffraction peaks can be observed. In contrast to the Joint Committee on Powder Diffraction Standard Cards (JCPDS-42-1450), these diffraction peaks can be indexed to the (111), (022), (113), (004), (224), (115) and (044) planes of cubic-phase CuCo₂S₄. It should be mentioned that the diffraction peaks of CuCo₂S₄ are very similar to that of Co₃S₄ because both of them possess the spinel structure. For distinguishing and confirming the composition of our sample, EDS and Raman spectroscopies are further carried out. The EDS pattern (Fig. S1†) proves the existence of Cu, Co and S elements with an atomic ratio close to 1 : 2 : 4. And the related Raman spectrum (Fig. 1B) shows the obvious vibrational peaks for the Co–S bond (200–400 cm^{-1}) and the Cu–S bond (400–1000 cm^{-1}), which is different from

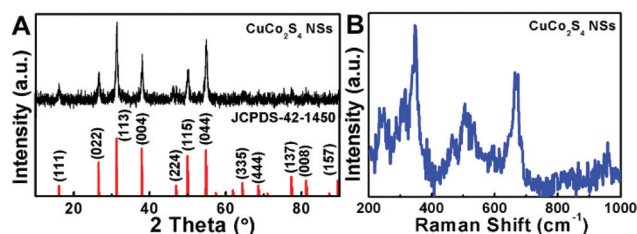


Fig. 1 (A) XRD pattern and (B) Raman spectrum of the as-synthesized CuCo₂S₄ NSs. The red column lines in (A) show the diffraction peaks of bulk CuCo₂S₄ (JCPDS-42-1450).

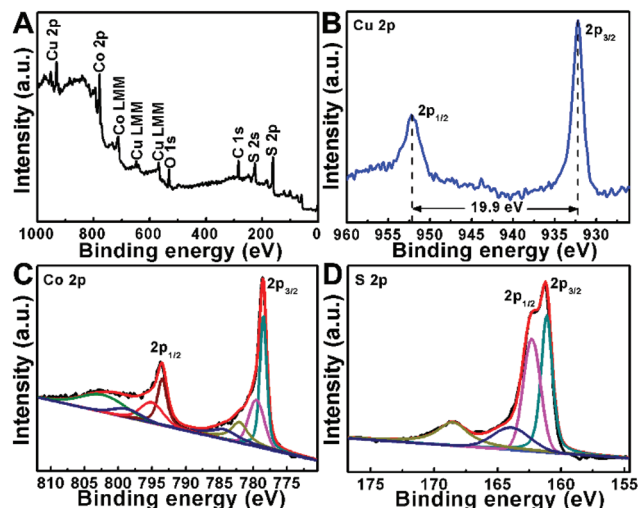


Fig. 2 (A) The survey XPS spectrum of CuCo_2S_4 NSs. (B–D) Corresponding fine XPS spectra for Cu 2p, (C) Co 2p, and (D) S 2p, respectively.

those of reported bulk Co_3S_4 and Co_2S_4 NSs.⁶ To further identify the component and valence states of Cu, Co and S elements, the XPS tests are also performed. The survey XPS spectrum (Fig. 2A) verifies the presence of Cu, Co, and S elements in our sample, consistent with the XRD, EDS, and Raman results. From the fine spectrum of Cu 2p (Fig. 2B), the binding energies (BEs) at 952.1 and 932.2 eV can be assigned to the spin-orbit doublets for the $2p_{1/2}$ and $2p_{3/2}$ peaks of Cu(I) ions ($\Delta E = 19.9$ eV),⁶⁴ in accordance with the previous report on the oxidation state of Cu in CuCo_2S_4 .²⁸ And from the Co 2p fine spectrum (Fig. 2C), the BEs at 795.3 and 779.6 eV are assigned to the spin-orbit doublets for the $2p_{1/2}$ and $2p_{3/2}$ peaks of Co(II) ions. And the BEs at 793.5 and 778.5 eV are attributed to the spin-orbit doublets for the $2p_{1/2}$ and $2p_{3/2}$ peaks of Co(III) ions. Besides these four peaks, other small peaks are the characteristic satellite peaks of Co(II) and Co(III) ions. This result reveals that the Co in the sample exhibits the valence states of +2 and +3, consistent with that of previous reports on cobalt-based spinel-structured compounds.⁶⁵ While for the S 2p fine spectrum (Fig. 2D), the BEs at 162.3 and 161.1 eV are the spin-orbit doublet for $2p_{1/2}$ and $2p_{3/2}$ peaks of S^{2-} ions.⁶⁶ Further evidence comes from the shakeup satellite peak at the BE of 168.5 eV. It should be mentioned that the $2p_{1/2}$ peak for S^{2-} ions is partially overlapped with that of S_2^{2-} ions.⁶⁷ That is to say, the valence state of S may be the coexistence of -2 and -1 . Additionally, the BE at 163.8 eV originates from DDT that is bound to Cu.⁶⁸

The morphology and microstructure of the CuCo_2S_4 NSs were examined using FE-SEM, AFM, TEM and HRTEM. From the FE-SEM image (Fig. 3A), large-area circular sheet-like nanostructures with a lateral size of ~ 100 – 200 nm are observed, revealing the formation of CuCo_2S_4 NSs. The AFM image and related height-profile patterns (Fig. S2†) indicate that the thickness of CuCo_2S_4 NSs is approximately 10–13 nm. The cor-

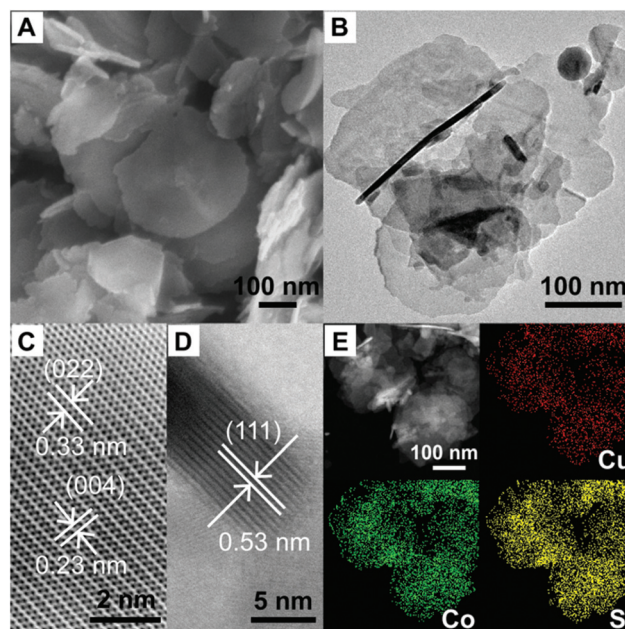


Fig. 3 (A) FE-SEM and (B) TEM images of the CuCo_2S_4 NSs. (C) The in-plane and (D) out-plane high resolution TEM images of an individual CuCo_2S_4 NS. (E) HAADF-STEM and element mapping images of CuCo_2S_4 NSs.

ponding low-magnification TEM image (Fig. 3B) further confirms that the obtained product possesses thin sheet-like motifs. To verify the exposed lattice planes, the in-plane and out-of-plane HRTEM images of an individual CuCo_2S_4 NS are collected. The in-plane HRTEM image (Fig. 3C) shows clear lattice fringes with the lattice spacings of approximately 0.33 and 0.23 nm, corresponding to the (022) and (004) planes of cubic-phase CuCo_2S_4 (JCPDS-42-1450), respectively. The out-of-plane HRTEM image (Fig. 3D) also exhibits clear lattice fringes with a lattice spacing of about 0.53 nm, assigned to the (111) plane of cubic phase CuCo_2S_4 (JCPDS-42-1450). These results demonstrate that the CuCo_2S_4 NSs mainly expose the (111), (022) and (004) planes. The high-angle annular dark field-scanning transmission electron microscopy (HAADF-STEM) and elemental-mapping images (Fig. 3E) verify that the elements Cu, Co and S are homogeneously distributed along the whole CuCo_2S_4 NS.

To gain insight into the growth mechanism of the CuCo_2S_4 NSs, a series of control experiments were carried out. The impact factors, such as the metal precursors and their ligands as well as the sulfur sources, were fully studied. Considering that acetate and nitrate have a similar means of coordination as acetylacetonate for Cu and Co ions, the two metal complexes ($\text{Cu}(\text{acac})_2$ and $\text{Co}(\text{acac})_2$) are replaced by the corresponding metal acetates and nitrates, respectively, while other conditions remain unchanged. As expected, using metal acetates as the precursors, the ternary CuCo_2S_4 NSs are obtained (Fig. S3A–C†) but their average sizes are smaller than those of the NSs synthesized by using acetylacetonate complexes as precursors. While using metal nitrates as the precursors, the ternary CuCo_2S_4 product can be obtained, but its shape is an

irregular polyhedron (Fig. S3D–F†). Additionally, when using metal chlorides instead of acetylacetonate complexes, only polyhedron-like nanostructures along with small nanoparticles of mixed binary metal sulfides are formed (Fig. S3G–I†). These facts reveal that metal precursors with distinct ligands not only modulate the reactivity of Cu and Co ions but also affect the crystallographic growth of the product. In our work, Cu- and Co-based acetylacetonate complexes are found to be the optimal precursors because they can effectively level the reactivity of metal ions to induce homogeneous nucleation and mediate the dynamic growth process, helpful to form phase-pure CuCo_2S_4 NSs. Except for the metal precursors, the sulfur sources also show a great influence on the morphology of the product. For instance, using sulfur powder or thioacetamide to replace DDT while other conditions remain constant, small CuCo_2S_4 nanoparticles are produced (Fig. S4†) instead of NSs. This result implies that DDT not only serves as a sulfur source but also acts as a structure-directing reagent.⁶⁹ Combined with the HRTEM results, it can be deduced that DDT may selectively adsorb on the (111) plane, which inhibits the growth along [111], facilitating the formation of a 2D crystal. Thus, we name our method as a “levelling metal activity and structure-directed one-pot sulfurization” strategy. The detailed growth mechanism for CuCo_2S_4 NSs is not fully clear at present and further work is underway. To highlight the significance of ternary CuCo_2S_4 NSs, pure binary metal sulfide nanostructures, including Cu_7S_4 nanodisks and Co_3S_4 nanocrystals, are also prepared under the same system. The related TEM images, XRD and EDS patterns, and Raman spectra are given in Fig. S5.†

The electrocatalytic properties of the CuCo_2S_4 NSs are firstly evaluated by using the ORR as the probe reaction. For comparison, Cu_7S_4 nanodisks and Co_3S_4 nanocrystals, and commercial Pt/C are used as the control catalysts. Fig. 4A shows the ORR

polarization curves of CuCo_2S_4 NSs and the other three control catalysts in O_2 -saturated 0.1 M KOH aqueous solution at a rotation rate of 1600 rpm. The onset potential and half-wave potential of CuCo_2S_4 NSs for the ORR are approximately 0.90 V and 0.74 V (vs. RHE), respectively, which are much higher than those of binary metal sulfides and other reported ORR catalysts (e.g., delithiated $\text{Li}_{1-x}\text{CoO}_2$, defective TiO_2 , $\text{Pd-H}_3\text{PW}_{12}\text{O}_{40}\text{-CMK3}$);^{70–72} comparable to Co, N-doped porous carbon⁷³ and Fe-Phen@MOF- ArNH_3 ,⁷⁴ and slightly lower than those of Pt/C. These results indicate that CuCo_2S_4 NSs are effective for the ORR in alkaline media, the activity of which is close to Pt/C, and much better than binary metal sulfides. In contrast to binary metal sulfides, the improved activity of ternary CuCo_2S_4 NSs may result from the component effect and efficient electronic coupling of the two metal cations with unique oxidation states (+1 for Cu, +2.4 for Co) as well as the formation of unique 2D geometric structures, which can enhance electric conductivity and offer more available active sites or crystal planes for the ORR.^{25,51,75} To further understand the catalytic behaviours of CuCo_2S_4 NSs, electrocatalytic dynamic tests are performed. Based on the ORR polarization curves at different rotation rates (Fig. 4B), the number of transferred electrons (n) involved in the ORR process is calculated according to the Koutecky–Levich (K–L) equation.⁷⁶ The good linearity of the K–L plots at different potentials (Fig. 4C) indicates that the ORR behavior of CuCo_2S_4 NSs follows the first-order kinetics. From the slopes of the K–L plots, the values of n at different potentials are very close to 4.0, implying that the ORR of CuCo_2S_4 NSs follows the four-electron pathway ($\text{O}_2 + 2\text{H}_2\text{O} + 4\text{e}^- \rightarrow 4\text{OH}^-$). In addition, their ORR kinetics are further evaluated by the Tafel plots (Fig. S6†). Compared with that of Pt/C (70 mV dec^{-1}), CuCo_2S_4 NSs show a comparable Tafel slope (74 mV dec^{-1}), indicating that the ORR kinetics of CuCo_2S_4 NSs are close to Pt/C. Since the durability of a catalyst is of significance for application, the electrocatalytic stability of CuCo_2S_4 NSs (Fig. 4D) is also examined by a chronoamperometric method at a constant potential of 0.6 V (vs. RHE). After continuously cycling for 10 h, 80.4% of the initial current density is reserved on CuCo_2S_4 NSs while only 66.7% of the initial current density is retained on Pt/C, implying that the durability of the former is higher than that of the latter. By performing TEM, Raman and XRD analysis of the samples after cycling tests (Fig. S7†), the ORR activity loss of CuCo_2S_4 NSs may originate from the large morphology variation along with slight oxidation to form a small amount of Cu oxides on their surfaces under electrochemical cycling, leading to reduced electronic conductivity of the catalyst and decreased available active sites or crystal planes for the ORR.

Moreover, the electrocatalytic properties of the CuCo_2S_4 NSs are further examined by using the OER as the probe reaction. Fig. 5A shows the OER polarization curves of CuCo_2S_4 NSs, pure binary metal sulfide nanostructures and Pt/C catalysts at the potential ranging from 1.2 to 1.9 V (vs. RHE). The OER onset potential of CuCo_2S_4 NSs is identified to be 1.5 V (vs. RHE). In 0.1 M KOH solution (pH = 13), the onset overpotential (η) is calculated to be 0.262 V according to the equation:

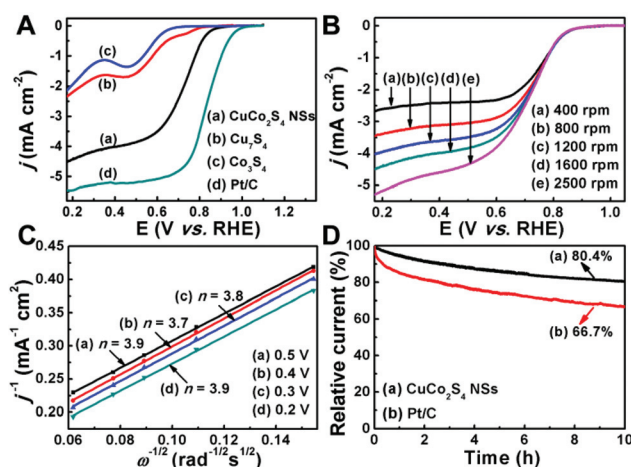


Fig. 4 (A) ORR polarization plots of the (a) CuCo_2S_4 NSs, (b) Cu_7S_4 nanodisks, (c) Co_3S_4 nanocrystals, and (d) Pt/C catalysts at a rotation rate of 1600 rpm. (B) Rotation rate dependent ORR polarization plots for CuCo_2S_4 NSs. (C) K–L plots of CuCo_2S_4 NSs and the number of transferred electrons at different potentials. (D) Chronoamperometric plots for (a) CuCo_2S_4 NSs and (b) Pt/C catalyst at a constant potential of 0.6 V (vs. RHE).

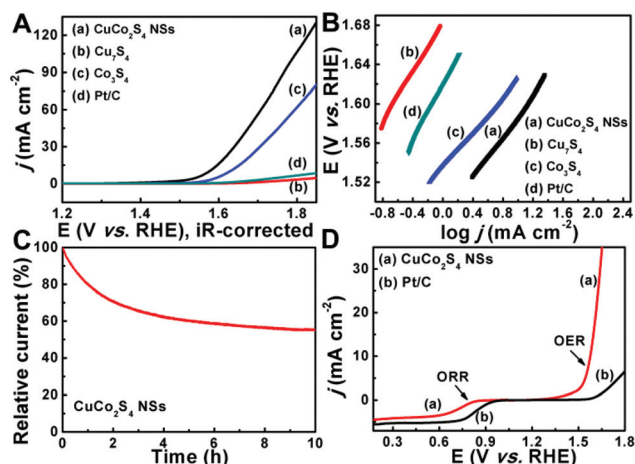


Fig. 5 (A) OER polarization plots and (B) Tafel plots of the (a) CuCo₂S₄ NSs, (b) Cu₇S₄ nanodisks, (c) Co₃S₄ nanocrystals, and (d) Pt/C catalysts. (C) Chronoamperometric plot for CuCo₂S₄ NSs at a constant potential of 1.6 V (vs. RHE). (D) Comparison of the bifunctional catalytic activity of (a) CuCo₂S₄ NSs with (b) Pt/C catalysts.

$\eta = E(V \text{ vs. RHE}) - 1.238 \text{ V}$, which is smaller than that of the Cu₇S₄ nanodisks (0.382 V), Co₃S₄ nanocrystals (0.322 V) and Pt/C (0.362 V) catalysts. This indicates that CuCo₂S₄ NSs are the best one for the OER among these examined catalysts. Except for the OER onset overpotential, the overpotential at a current density of 10 mA cm^{-2} ($\eta_{10 \text{ mA cm}^{-2}}$) usually serves as a key benchmark to evaluate the activity of OER electrocatalysts.⁷⁷ The $\eta_{10 \text{ mA cm}^{-2}}$ of CuCo₂S₄ NSs is 0.337 V, which is lower than that of Co₃S₄ nanocrystals (0.390 V) and Pt/C (0.645 V), and some other reported OER catalysts, such as Au@Co₃O₄ (0.420 V),⁷⁸ Ni@ [Ni_(2+/3+)Co₂(OH)₆₋₇]_x nanotubes (0.460 V),⁷⁹ Mn₃O₄/CoSe₂ nanocomposites (0.360 V),⁸⁰ and NiCoO_x films (0.380 V).⁸¹ Moreover, the $\eta_{10 \text{ mA cm}^{-2}}$ value of CuCo₂S₄ NSs is comparable to reported Ni-Fe-LDH/N-doped graphene nano-hybrids (0.337 V)⁸² and LiCo_{0.8}Fe_{0.2}O₂ powders (0.340 V).⁸³ Based on the OER polarization curves of these catalysts, the related Tafel plots (η - $\log j$) are obtained (Fig. 5B) to evaluate their OER kinetics. From the calculated Tafel slope values, the OER kinetics of CuCo₂S₄ NSs are close to Co₃S₄ nanocrystals while superior to Cu₇S₄ nanodisks and Pt/C. Moreover, the durability of CuCo₂S₄ NSs for the OER is further evaluated using a chronoamperometric method at a potential of 1.6 V (vs. RHE). As shown in Fig. 5C, the CuCo₂S₄ NSs can reserve only 55.1% of the initial current density after continuously working for 10 h. By performing the cycling tests many times and collecting the samples for TEM, XRD and XPS analysis (Fig. S8†), the poor stability of CuCo₂S₄ NSs for the OER may result from the generation of amorphous oxides on their surfaces under continuous electrochemical cycling that reduce the available catalytic active sites.

The ORR and OER tests suggest that CuCo₂S₄ NSs are promising bifunctional oxygen-electrode catalysts in alkaline media. Usually, the bifunctional catalytic activity is evaluated by the potential drop (ΔE) between the OER current density at 10 mA

cm^{-2} ($E_{10 \text{ mA cm}^{-2}, \text{OER}}$) and either the ORR current density at -3 mA cm^{-2} ($E_{-3 \text{ mA cm}^{-2}, \text{ORR}}$)⁸⁴ or the ORR current density at the half-wave position ($E_{1/2, \text{ORR}}$).⁸⁵ Smaller ΔE values mean better bifunctional catalytic activity and greater potential for practical application. Here, the ΔE value is calculated according to the equation: $\Delta E = E_{10 \text{ mA cm}^{-2}, \text{OER}} - E_{1/2, \text{ORR}}$ and is employed for evaluating the bifunctional catalytic activity of CuCo₂S₄ NSs. Among the three sulfide catalysts, the CuCo₂S₄ NSs exhibit the smallest $E_{10 \text{ mA cm}^{-2}, \text{OER}}$ and the maximal $E_{1/2, \text{ORR}}$, and hence the smallest ΔE with a value of 0.835 V is obtained (Fig. S9†). Such a ΔE value is also smaller than those for some other reported bifunctional catalysts (e.g. Co_xS_y@C-1000, N-doped G/CNTs, Co₃O₄/NBGHSS, CoFe₂O₄, Co_xMn_{3-x}O₄, LaCoO_{3- δ} , MnO_x, NiCo₂S₄ hollow spheres, NiCo₂S₄@N/S-rGO, Co₃O₄/2.7Co₂MnO₄, Ni_{0.6}Co_{2.4}O₄, MnCo₂O₄/C, LDO/CNTs, N-doped G mesh, delithiated Li_{1-x}CoO₂).^{43-45,47-58,70} The main parameters of our CuCo₂S₄ NSs and currently reported bifunctional catalysts are listed in Table S1,† from which we can see that CuCo₂S₄ NSs show the best performance in the current family of spinel-structured bifunctional oxygen electrocatalysts. Remarkably, in contrast to Pt/C ($\Delta E = 1.053 \text{ V}$) and other CuCo₂S₄ nanostructures obtained by using different metal precursors or sulfur sources, the CuCo₂S₄ NSs also exhibit the smallest ΔE value (Fig. 5D, S10 and Table S2†), indicating that CuCo₂S₄ NSs may serve as a promising bifunctional catalyst for regenerative alkaline H₂-O₂ fuel cells or metal-air batteries.

To understand the underlying mechanism of the good bifunctional catalytic properties of CuCo₂S₄ NSs, spin-polarized DFT computations are further carried out. Generally, in alkaline media, the ORR process involves the following four steps: (1) $\text{O}_2 + \text{H}_2\text{O} + \text{e}^- + * \rightarrow \text{OOH}^* + \text{OH}^-$; (2) $\text{OOH}^* + \text{e}^- \rightarrow \text{O}^* + \text{OH}^-$; (3) $\text{O}^* + \text{H}_2\text{O} + \text{e}^- \rightarrow \text{OH}^* + \text{OH}^-$; (4) $\text{OH}^* + \text{e}^- \rightarrow * + \text{OH}^-$; where $*$ denotes an adsorption site.^{86,87} While for the OER, its approach in an alkaline environment can be represented as: (1) $* + \text{OH}^- \rightarrow \text{OH}^* + \text{e}^-$; (2) $\text{OH}^* + \text{OH}^- \rightarrow \text{O}^* + \text{H}_2\text{O} + \text{e}^-$; (3) $\text{O}^* + \text{OH}^- \rightarrow \text{OOH}^* + \text{e}^-$; (4) $\text{OOH}^* + \text{OH}^- \rightarrow \text{O}_2 + \text{H}_2\text{O} + \text{e}^- + *$.⁸⁸ From the thermodynamic point, the ORR/OER performance of a desired catalyst can be well quantified by the estimated reaction overpotential (η), of which a lower value means a better catalyst, since an ideal catalyst could facilitate the catalytic process at the equilibrium potential (that is $\eta = 0$). Theoretically, the overpotential^{89,90} is relative to the free energy changes (ΔG) of electron reaction pathways, and hence the ΔG of each step is calculated on the basis of the CHE model,⁸⁹ which has been widely utilized to elucidate electrochemical reaction pathways with the consideration of voltage requirements. Combined with HRTEM analysis, the mainly exposed surfaces, namely (111), (022), and (004) planes, are selected as the active surface for computations. Note that the most stable termination has been chosen for each studied surface, and the (004) plane is the most stable among them, followed by (111) and (022). According to our calculations (for the details please see the ESI†), it is found that the (111) plane shows poor catalytic performance because of its quite strong adsorption for adsorbates (Fig. S11A and B†), while (022) and

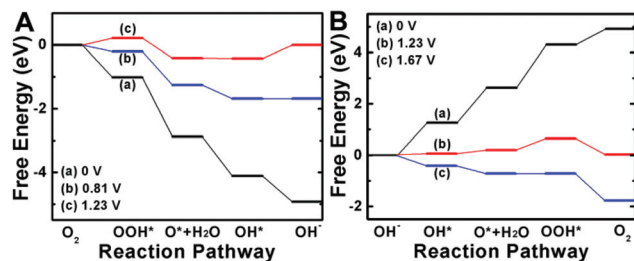


Fig. 6 (A, B) The free energy profile for the ORR pathway on the (022) plane (A) and the OER pathway on the (004) plane (B) at different potentials. The black, red, and blue lines represent the zero potential, the equilibrium potential, and the limiting potential, respectively.

(004) planes are in favour of the ORR and OER, respectively. Fig. 6A lists the free energy changes during the ORR on the (022) surface at different potentials (U). According to the CHE model, all ORR steps are spontaneously exothermic at zero potential and still downhill at 0.81 V. However, when U is higher than 0.81 V, the last electrochemical step would be endothermic, indicating that the key step in the ORR on the (022) plane is the reduction of OH^* to OH^- . On the other hand, the free energy profile for the OER over the (004) facet is provided in Fig. 6B. It is shown that the OER process on the (004) plane needs a potential of 1.67 V to become exergonic and is limited by conversion of O^* to OOH^* . So, the (022) plane shows superior ORR activity, while the (004) plane is in favour of the OER process. We also note here that the theoretical overpotentials of CuCo_2S_4 NSs for the ORR and OER are 0.42 V and 0.44 V, respectively, lower than those of some superior ORR/OER catalysts identified theoretically, such as Pt (0.45 V for the ORR)⁸⁹ and IrO_2 (0.58 V for the OER),⁹⁰ which are consistent with our experimental tests. Moreover, our calculations demonstrated that (022) and (004) planes exhibit comparable catalytic activity for the OER (Fig. S11C†) and ORR (Fig. S11D†), respectively, which further enhance the bifunctional activity. Overall, based on the above analysis, we can conclude that the excellent bifunctional catalytic activity of CuCo_2S_4 NSs may result from the presence of (022) and (004) facets that have different preferences in terms of the ORR/OER.

Conclusions

In summary, novel 2D crystals of non-layered thiospinel compound- CuCo_2S_4 NSs-with their (111), (022) and (004) planes mainly exposed, have been synthesized *via* a “levelling metal reactivity and structure-directed one-pot sulfurization” strategy. The average thickness of the obtained CuCo_2S_4 NSs is about 10–13 nm. Such NSs show excellent bifunctional catalytic properties toward both ORR and OER in alkaline media, which are superior to binary metal sulfides, Pt/C and CuCo_2S_4 nanoparticles, and recently reported bifunctional oxygen electrocatalysts (*e.g.*, $\text{Co}_x\text{S}_y\text{@C-1000}$, N-doped G/CNTs, $\text{Co}_3\text{O}_4/\text{NBGHSS}$, CoFe_2O_4 , $\text{Co}_x\text{Mn}_{3-x}\text{O}_4$, $\text{LaCoO}_{3-\delta}$, MnO_x , NiCo_2S_4 hollow

spheres, $\text{NiCo}_2\text{S}_4\text{@N/S-rGO}$, $\text{Co}_3\text{O}_4/2.7\text{Co}_2\text{MnO}_4$, $\text{Ni}_{0.6}\text{Co}_{2.4}\text{O}_4$, $\text{MnCo}_2\text{O}_4/\text{C}$, $\text{Li}_{1-x}\text{CoO}_2$, *etc.*). It should be mentioned that their durability for the OER needs to be improved by suppressing surface oxidation. As revealed by spin-polarized DFT computations based on CHE model, their excellent bifunctional catalytic properties result from the exposure of two special planes, (022) and (004), which have different preferences in terms of ORR/OER. This work not only enriches the current 2D crystal family but also paves the way for rational design of advanced multifunctional 2D electrocatalysts to apply in many renewable energy options. Further work on encapsulating CuCo_2S_4 NSs with N,S-doped porous carbon or other materials to suppress surface oxidation and form advanced core-shell nanohybrid electrocatalyst is underway.

Conflict of interest

The authors declare no competing financial interest.

Authors contribution

The manuscript was written through contributions of all authors. All authors have given approval for the final version of the manuscript.

Acknowledgements

We gratefully acknowledge financial support from the National Natural Science Foundation of China (21271105, 21522305, 21541007, and 21671106), research funds from the Priority Academic Program Development of Jiangsu Higher Education Institutions and the Natural Science Project of Jiangsu Province (BK20150045). M. Han greatly thanks Prof. H. Zhang (Nanyang Technol. Univ.) for discussing the experimental results. Also, M. Han thanks Dr X. Wu, Dr B. Chen, Dr X. Zhang, and Dr Z. Luo for giving valuable suggestions to revise this paper.

Notes and references

- 1 M. Chhowalla, H. S. Shin, G. Eda, L. J. Li, K. P. Loh and H. Zhang, *Nat. Chem.*, 2013, **5**, 263.
- 2 X. Zhang and Y. Xie, *Chem. Soc. Rev.*, 2013, **42**, 8187.
- 3 S. Lei, F. Wen, B. Li, Q. Wang, Y. Huang, Y. Gong, Y. He, P. Dong, J. Bellah, A. George, L. Ge, J. Lou, N. J. Halas, R. Vajtai and P. M. Ajayan, *Nano Lett.*, 2015, **15**, 259.
- 4 M. Acerce, D. Voiry and M. Chhowalla, *Nat. Nanotechnol.*, 2015, **10**, 313.
- 5 Y. Zhang, B. Zheng, C. Zhu, X. Zhang, C. Tan, H. Li, B. Chen, J. Yang, J. Chen, Y. Huang, L. Wang and H. Zhang, *Adv. Mater.*, 2015, **27**, 935.
- 6 Y. Liu, C. Xiao, M. Lyu, Y. Lin, W. Cai, P. Huang, W. Tong, Y. Zou and Y. Xie, *Angew. Chem., Int. Ed.*, 2015, **127**, 11383.

- 7 M. Asadi, K. Kim, C. Liu, A. V. Addepalli, P. Abbasi, P. Yasaei, P. Phillips, A. Behranginia, J. M. Cerrato, R. Haasch, P. Zapol, B. Kumar, R. F. Klie, J. Abiade, L. A. Curtiss and A. Salehi-Khojin, *Science*, 2016, **353**, 467.
- 8 J. Xie, H. Zhang, S. Li, R. Wang, X. Sun, M. Zhou, J. Zhou, X. W. Lou and Y. Xie, *Adv. Mater.*, 2013, **25**, 5807.
- 9 D. Voiry, H. Yamaguchi, J. Li, R. Silva, D. C. Alves, T. Fujita, M. Chen, T. Asefa, V. B. Shenoy, G. Eda and M. Chhowalla, *Nat. Mater.*, 2013, **12**, 850.
- 10 A. Y. Eng, A. Ambrosi, Z. Sofer, P. Simek and M. Pumera, *ACS Nano*, 2014, **8**, 12185.
- 11 H. Zhang, *ACS Nano*, 2015, **9**, 9451.
- 12 J. Xie, J. Zhang, S. Li, F. Grote, X. Zhang, H. Zhang, R. Wang, Y. Lei, B. Pan and Y. Xie, *J. Am. Chem. Soc.*, 2013, **135**, 17881.
- 13 J. Xie and Y. Xie, *ChemCatChem*, 2015, **7**, 2568.
- 14 Z. Li, X. Dou, Y. Zhao and C. Wu, *Inorg. Chem. Front.*, 2016, **3**, 1021.
- 15 J. Xie, S. Li, X. Zhang, J. Zhang, R. Wang, H. Zhang, B. Pan and Y. Xie, *Chem. Sci.*, 2014, **5**, 4615.
- 16 P. Chen, K. Xu, Y. Tong, X. Li, S. Tao, Z. Fang, W. Chu, X. Wu and C. Wu, *Inorg. Chem. Front.*, 2016, **3**, 236.
- 17 J. Xie and Y. Xie, *Chem. – Eur. J.*, 2016, **22**, 3588.
- 18 J. Xie, J. Xin, G. Cui, X. Zhang, L. Zhou, Y. Wang, W. Liu, C. Wang, M. Ning, X. Xia, Y. Zhao and B. Tang, *Inorg. Chem. Front.*, 2016, **3**, 1160.
- 19 J. Xie, R. Wang, J. Bao, X. Zhang, H. Zhang, S. Li and Y. Xie, *Inorg. Chem. Front.*, 2014, **1**, 751.
- 20 J. A. Carrasco, J. Romero, M. Varela, F. Hauke, G. Abellán, A. Hirsch and E. Coronado, *Inorg. Chem. Front.*, 2016, **3**, 478.
- 21 M. Jiang, Y. Li, Z. Lu, X. Sun and X. Duan, *Inorg. Chem. Front.*, 2016, **3**, 630.
- 22 Q. Gong, L. Cheng, C. Liu, M. Zhang, Q. Feng, H. Ye, M. Zeng, L. Xie, Z. Liu and Y. Li, *ACS Catal.*, 2015, **5**, 2213.
- 23 Q. Fu, L. Yang, W. Wang, A. Han, J. Huang, P. Du, Z. Fan, J. Zhang and B. Xiang, *Adv. Mater.*, 2015, **27**, 4732.
- 24 I. Naik, C. S. Yadav and A. K. Rastogi, *Phys. Rev. B: Condens. Matter*, 2007, **75**, 115112.
- 25 Y. Sun, S. Gao, F. Lei, J. Liu, L. Liang and Y. Xie, *Chem. Sci.*, 2014, **5**, 3976.
- 26 F. Song and X. Hu, *Nat. Commun.*, 2014, **5**, 4477.
- 27 C. Tan and H. Zhang, *Nat. Commun.*, 2015, **6**, 7873.
- 28 R. A. D. Patrick, V. S. Coker, C. I. Pearce, N. D. Telling and G. van der Laan, *Can. Mineral.*, 2008, **46**, 1317.
- 29 R. J. Bouchard, P. A. Russo and A. Wold, *Inorg. Chem.*, 1965, **4**, 685.
- 30 M. Eisenberg, *J. Electrochem. Soc.*, 1980, **127**, 2382.
- 31 M. M. Thackeray, L. A. de Picciotto, A. de Kock, P. J. Johnson, V. A. Nicholas and K. T. Adendorff, *J. Power Sources*, 1987, **21**, 1.
- 32 J. Tang, Y. Ge, J. Shen and M. Ye, *Chem. Commun.*, 2016, **52**, 1509.
- 33 S. E. Moosavifard, S. Fani and M. Rahmanian, *Chem. Commun.*, 2016, **52**, 4517.
- 34 J. Shen, J. Tang, P. Dong, Z. Zhang, J. Ji, R. Baines and M. Ye, *RSC Adv.*, 2016, **6**, 13456.
- 35 Q. Luo, Y. Gu, J. Li, N. Wang and H. Lin, *J. Power Sources*, 2016, **312**, 93.
- 36 A. M. Wiltrout, C. G. Read, E. M. Spencer and R. E. Schaak, *Inorg. Chem.*, 2016, **55**, 221.
- 37 X. Wang, Y. Ke, H. Pan, K. Ma, Q. Xiao, D. Yin, G. Wu and M. T. Swihart, *ACS Catal.*, 2015, **5**, 2534.
- 38 M. Zhang, M. de Respinis and H. Frei, *Nat. Chem.*, 2014, **6**, 362.
- 39 J. Bao, X. Zhang, B. Fan, J. Zhang, M. Zhou, W. Yang, X. Hu, H. Wang, B. Pan and Y. Xie, *Angew. Chem., Int. Ed.*, 2015, **54**, 7399.
- 40 H. S. Ahn, J. Yano and T. D. Tilley, *ACS Catal.*, 2015, **5**, 2573.
- 41 X. Cao, X. Zheng, J. Tian, C. Jin, K. Ke and R. Yang, *Electrochim. Acta*, 2016, **191**, 776.
- 42 X. Li, Y. Fang, S. Zhao, J. Wu, F. Li, M. Tian, X. Long, J. Jin and J. Ma, *J. Mater. Chem. A*, 2016, **4**, 13133.
- 43 B. Chen, R. Li, G. Ma, X. Gou, Y. Zhu and Y. Xia, *Nanoscale*, 2015, **7**, 20674.
- 44 G. L. Tian, M. Q. Zhao, D. Yu, X. Y. Kong, J. Q. Huang, Q. Zhang and F. Wei, *Small*, 2014, **10**, 2251.
- 45 Z. Jiang, Z. J. Jiang, T. Maiyalagan and A. Manthiram, *J. Mater. Chem. A*, 2016, **4**, 5877.
- 46 S. R. Alvarado, Y. Guo, T. P. A. Ruberu, E. Tavasoli and J. Vela, *Coord. Chem. Rev.*, 2014, **263**, 182.
- 47 A. Indra, P. W. Menezes, N. R. Sahraie, A. Bergmann, C. Das, M. Tallarida, D. Schmeisser, P. Strasser and M. Driess, *J. Am. Chem. Soc.*, 2014, **136**, 17530.
- 48 F. Cheng, J. Shen, B. Peng, Y. Pan, Z. Tao and J. Chen, *Nat. Chem.*, 2011, **3**, 79.
- 49 J. I. Jung, H. Y. Jeong, J. S. Lee, M. G. Kim and J. Cho, *Angew. Chem., Int. Ed.*, 2014, **53**, 4582.
- 50 Y. Meng, W. Song, H. Huang, Z. Ren, S. Y. Chen and S. L. Suib, *J. Am. Chem. Soc.*, 2014, **136**, 11452.
- 51 M. Wang, Y. Lai, J. Fang, F. Qin, Z. Zhang, J. Li and K. Zhang, *Catal. Sci. Technol.*, 2016, **6**, 434.
- 52 Q. Liu, J. Jin and J. Zhang, *ACS Appl. Mater. Interfaces*, 2013, **5**, 5002.
- 53 D. Wang, X. Chen, D. G. Evans and W. Yang, *Nanoscale*, 2013, **5**, 5312.
- 54 T. N. Lambert, J. A. Vigil, S. E. White, D. J. Davis, S. J. Limmer, P. D. Burton, E. N. Coker, T. E. Beechem and M. T. Brumbach, *Chem. Commun.*, 2015, **51**, 9511.
- 55 K. L. Pickrahn, S. W. Park, Y. Gorlin, H.-B.-R. Lee, T. F. Jaramillo and S. F. Bent, *Adv. Energy Mater.*, 2012, **2**, 1269.
- 56 P. W. Menezes, A. Indra, N. R. Sahraie, A. Bergmann, P. Strasser and M. Driess, *ChemSusChem*, 2015, **8**, 164.
- 57 H.-F. Wang, C. Tang, X. Zhu and Q. Zhang, *J. Mater. Chem. A*, 2016, **4**, 3379.
- 58 C. Tang, H. F. Wang, X. Chen, B. Q. Li, T. Z. Hou, B. Zhang, Q. Zhang, M. M. Titirici and F. Wei, *Adv. Mater.*, 2016, **28**, 6845.
- 59 X. Zhong, Y. Jiang, X. Chen, L. Wang, G. Zhuang, X. Li and J.-G. Wang, *J. Mater. Chem. A*, 2016, **4**, 10575.

- 60 Y. R. Zheng, M. R. Gao, Q. Gao, H. H. Li, J. Xu, Z. Y. Wu and S. H. Yu, *Small*, 2015, **11**, 182.
- 61 G. Kresse and J. Hafner, *Phys. Rev. B: Condens. Matter*, 1993, **47**, 558.
- 62 J. P. Perdew, K. Burke and M. Ernzerhof, *Phys. Rev. Lett.*, 1996, **77**, 3865.
- 63 G. Kresse and D. Joubert, *Phys. Rev. B: Condens. Matter*, 1999, **59**, 1758.
- 64 P. Dai, X. Shen, Z. Lin, Z. Feng, H. Xu and J. Zhan, *Chem. Commun.*, 2010, **46**, 5749.
- 65 J. Li, S. Xiong, Y. Liu, Z. Ju and Y. Qian, *ACS Appl. Mater. Interfaces*, 2013, **5**, 981.
- 66 J. Xiao, L. Wan, S. Yang, F. Xiao and S. Wang, *Nano Lett.*, 2014, **14**, 831.
- 67 A. N. Buckley, W. M. Skinner, S. L. Harmer, A. Pring and L.-J. Fan, *Geochim. Cosmochim. Acta*, 2009, **73**, 4452.
- 68 P. L. Saldanha, R. Brescia, M. Prato, H. Li, M. Povia, L. Manna and V. Lesnyak, *Chem. Mater.*, 2014, **26**, 1442.
- 69 J. Wang, J. Liu, H. Xu, S. Ji, J. Wang, Y. Zhu, P. Hodfson and Y. Li, *J. Mater. Chem. A*, 2013, **1**, 1117.
- 70 T. Maiyalagan, K. A. Jarvis, S. Therese, P. J. Ferreira and A. Manthiram, *Nat. Commun.*, 2014, **5**, 3949.
- 71 D. N. Pei, L. Gong, A. Y. Zhang, X. Zhang, J. J. Chen, Y. Mu and H. Q. Yu, *Nat. Commun.*, 2015, **6**, 8696.
- 72 H. Liu, Y. Zheng, G. Wang and S. Z. Qiao, *Adv. Energy Mater.*, 2015, **5**, 1401186.
- 73 Y. Z. Chen, C. Wang, Z. Y. Wu, Y. Xiong, Q. Xu, S. H. Yu and H. L. Jiang, *Adv. Mater.*, 2015, **27**, 5010.
- 74 K. Strickland, E. Miner, Q. Jia, U. Tylus, N. Ramaswamy, W. Liang, M. T. Sougrati, F. Jaouen and S. Mukerjee, *Nat. Commun.*, 2015, **6**, 7343.
- 75 A. C. Tavares, M. A. M. Cartaxo, M. I. da Silva Pereira and F. M. Costa, *J. Electroanal. Chem.*, 1999, **464**, 187–197.
- 76 K. Parvez, S. Yang, Y. Hernandez, A. Winter, A. Turchanin, X. Feng and K. Müllen, *ACS Nano*, 2012, **6**, 9541.
- 77 Y. Gorlin and T. F. Jaramillo, *J. Am. Chem. Soc.*, 2010, **132**, 13612.
- 78 Z. Zhuang, W. Sheng and Y. Yan, *Adv. Mater.*, 2014, **26**, 3950.
- 79 Z. Zhao, H. Wu, H. He, X. Xu and Y. Jin, *Adv. Funct. Mater.*, 2014, **24**, 4698.
- 80 M. R. Gao, Y. F. Xu, J. Jiang, Y. R. Zheng and S. H. Yu, *J. Am. Chem. Soc.*, 2012, **134**, 2930.
- 81 C. C. McCrory, S. Jung, J. C. Peters and T. F. Jaramillo, *J. Am. Chem. Soc.*, 2013, **135**, 16977.
- 82 C. Tang, H. S. Wang, H. F. Wang, Q. Zhang, G. L. Tian, J. Q. Nie and F. Wei, *Adv. Mater.*, 2015, **27**, 4516.
- 83 Y. Zhu, W. Zhou, Y. Chen, J. Yu, M. Liu and Z. Shao, *Adv. Mater.*, 2015, **27**, 7150.
- 84 P. Ganesan, M. Prabu, J. Sanetuntikul and S. Shanmugam, *ACS Catal.*, 2015, **5**, 3625.
- 85 Y. Wang, W. Ding, S. Chen, Y. Nie, K. Xiong and Z. Wei, *Chem. Commun.*, 2014, **50**, 15529.
- 86 Y. Jiao, Y. Zheng, M. Jaroniec and S. Z. Qiao, *J. Am. Chem. Soc.*, 2014, **136**, 4394.
- 87 J. Zhang, Z. Zhao, Z. Xia and L. Dai, *Nat. Nanotechnol.*, 2015, **10**, 444.
- 88 X. Cui, P. Ren, D. Deng, J. Deng and X. Bao, *Energy Environ. Sci.*, 2016, **9**, 123.
- 89 J. K. Nørskov, J. Rossmeisl, A. Logadottir, L. Lindqvist, J. R. Kitchin, T. Bligaard and H. Jónsson, *J. Phys. Chem. B*, 2004, **108**, 17886.
- 90 I. C. Man, H.-Y. Su, F. Calle-Vallejo, H. A. Hansen, J. I. Martínez, N. G. Inoglu, J. Kitchin, T. F. Jaramillo, J. K. Nørskov and J. Rossmeisl, *ChemCatChem*, 2011, **3**, 1159.